Nanoscale

PAPER

View Article Online
View Journal | View Issue

Cite this: *Nanoscale*, 2023, **15**, 7318

Open Access Article. Published on 30 2023. Downloaded on 02-08-2024 18:17:53.
This article is licensed under a Creative Commons Attribution-NonCommercial 3.0 Unported Licence.

Quantum plasmonic two-dimensional WS_2–MoS_2 heterojunction†

Sharad Ambardar,[a] Zachary H. Withers,[b] Jiru Liu,[c] Xiaoyi Lai,[d] Abdullah Albagami,[e,f] Alina Zhukova,[f] Pedro Fabris Capelli,[f] Prasana K. Sahoo[g] and Dmitri V. Voronine[a,f]

Two-dimensional heterostructures have recently gained broad interest due to potential applications in optoelectronic devices. Their reduced dimensionality leads to novel physical effects beyond conventional bulk electronics. However, the optical properties of the 2D lateral heterojunctions have not been completely characterized due to the limited spatial resolution, requiring nano-optical techniques beyond the diffraction limit. Here, we investigate lateral monolayer WS_2–MoS_2 heterostructures in a plasmonic Au–Au tip–substrate picocavity using subdiffraction limited tip-enhanced photoluminescence (TEPL) spectroscopy with sub-nanometer tip–sample distance control. We observed more than 3 orders of magnitude PL enhancement by placing a plasmonic Au-coated tip at the resonantly excited heterojunction. We developed a theoretical model of the quantum plasmonic 2D heterojunction, where tunneling of hot electrons between the Au tip and MoS_2 leads to the quenching of the MoS_2 PL, while simultaneously increasing the WS_2 PL, in contrast to the non-resonant reverse transfer. Our simulations show good agreement with the experiments, revealing a range of parameters and enhancement factors corresponding to the switching between the classical and quantum regimes. The controllable photoresponse of the 2D heterojunction can be used in novel nanodevices.

Received 23rd February 2023,
Accepted 27th March 2023

DOI: 10.1039/d3nr00861d

rsc.li/nanoscale

Introduction

Lateral 2D heterostructures of transition metal dichalcogenides (TMDs) have been investigated due to the exceptional properties of their atomically sharp junctions, quantum confinement, and band gap tunability.[1–7] TMDs have been investigated for optoelectronic, sensing, and quantum information applications.[8–10] However, because of the highly averaged measurements of the far-field optical characterization experiments such as the conventional photoluminescence (PL) spectroscopy, there is a need to improve the understanding and applications of the heterojunctions at the nanoscale. This is experimentally challenging since the PL signals from the atomically thin junctions are weak and the surrounding materials generate large background. Previously, several nano-optical imaging techniques were used to address this challenge including scanning near-field optical microscopy (SNOM),[11,12] tip-enhanced Raman spectroscopy (TERS),[13–15] and tip-enhanced photoluminescence (TEPL).[16–18] The spatial imaging resolution in these techniques depends on the size of the excitation spot and the signal enhancement. The excitation spot size is limited by the size of the scanning local probe such as the plasmonic metallic tip, which is typically on the order of ~10 nm. The signal enhancement is limited by the electric field strength at the tip apex, which depends on tip–sample distance (TSD). Classically, the PL signal increases with the decrease of the TSD.[19] However, for the TSD shorter than ~1 nm, the PL signal decreases due to charge tunnelling between the tip and the sample, leading to the depletion of surface charge density, described using the quantum plasmonics model.[20–29]

Quantum effects, such as tunneling and non-locality, play an important role in plasmonic systems when the TSD is reduced. The classical descriptions of surface plasmon energy, linewidth, and field enhancement break down, and the full quantum mechanical treatment is necessary.[18,21–23,25,27–31] In this quantum plasmonic regime, tunneling at small TSD leads to the reduction of surface charge density and the corresponding near field intensity. Therefore, after the optimal

---

[a] Department of Medical Engineering, University of South Florida, Tampa, FL 33620, USA. E-mail: dmitri.voronine@gmail.com
[b] Department of Physics, Stony Brook University, Stony Brook, NY 11790, USA
[c] Department of Physics, Texas A&M University, College Station, TX 77840, USA
[d] CAS Center for Excellence and Synergetic Innovation Center in Quantum Information and Quantum Physics, University of Science and Technology of China, Hefei, Anhui 230026, China
[e] Department of Physics, King Saud University, Riyadh 11362, Kingdom of Saudi Arabia
[f] Department of Physics, University of South Florida, Tampa, FL 33620, USA
[g] Materials Science Centre, India Institute of Technology, Kharagpur, India

† Electronic supplementary information (ESI) available. See DOI: **https://doi.org/10.1039/d3nr00861d**

This journal is © The Royal Society of Chemistry 2023

Open Access Article. Published on 30 2023. Downloaded on 02-08-2024 18:17:53.
This article is licensed under a Creative Commons Attribution-NonCommercial 3.0 Unported Licence.

balance of EM enhancement and tunneling suppression, further reduction of TSD leads to the quenching of the TEPL signal. This specific value of TSD sets the quantum tunneling limit to TEPL that has traditionally been accepted as "ultimate".[32] Several experimental demonstrations revealed this tunneling limit of SERS signals for gaps smaller than ~1 nm.[22,33] Similar limits were shown in TSD dependence studies of TEPL.[27] These quantum plasmonic effects have been mainly investigated in pure TMD materials or the non-resonantly excited TMD heterostructures.[34] However, the TSD dependence of the PL in resonantly excited TMD heterostructures has not been investigated. Therefore, the limits of PL enhancement in such systems have not been well understood. TSD is a control parameter that can be optimized to obtain the maximum signal enhancement and the highest spatial resolution. It will provide a better understanding and controllability of the nanoscale quantum devices based on the complex interplay of excitons, plasmons and hot electrons.

Hot electrons, generated in plasmonic systems, contribute to the PL enhancement.[34,35] Hot electron injection (HEI) in TMDs promotes photoemission and photosensitive reactions.[36–38] Strong localized electromagnetic fields of plasmonic nanostructures facilitate HEI,[39–41] and can be optimized by varying TSD in the picoscale quantum tunneling regime. Previously, we investigated the TSD dependence of HEI in lateral WSe_2–$MoSe_2$ heterostructures excited above the band gap.[34] We observed $MoSe_2$ PL enhancement and WSe_2 PL quenching in the quantum tunneling regime of TSD < 1 nm due to the transfer of the injected electrons across the WSe_2–>$MoSe_2$ junction.

Here, we investigated a different 2D TMD system, namely, a WS_2–MoS_2 monolayer lateral heterostructure in a plasmonic cavity between a Au tip and an atomically thin Au substrate. We performed the picometer-scale controlled TSD dependent PL measurements using a 660 nm laser excitation, in resonance with the A excitons of the heterostructure. The experiments were carried out at several spatial locations across the junction in the classical (320 pm < TSD < 20 nm) and quantum tunnelling (220 pm < TSD < 320 pm) regimes. We calculated the corresponding classical and quantum PL enhancement factors, which showed more than 3 orders of magnitude PL intensity increase at the junction. We developed a phenomenological model of the quantum plasmonic lateral 2D heterojunction at various TSDs, which showed a good agreement with the experiments. This work provides new insights into the PL enhancement mechanisms of 2D lateral junctions and can be used for designing novel nanodevices.

Materials and methods

Monolayer lateral WS_2–MoS_2 heterostructures were grown on a SiO_2/Si substrate in a quartz tube using a one-pot chemical vapor deposition (CVD) system as previously described.[6] The heterostructures were transferred to an atomically flat Au substrate (TedPella) using a PMMA-assisted liquid transfer method.

AFM, PL and TEPL imaging were performed using a confocal optical microscope (LabRam Evolution, Horiba) coupled to a scanning probe microscope (OmegaScopeR, Horiba) as previously described.[26] Briefly, the 660 nm or 532 nm linearly polarized laser excitation beams were focused on the tip apex of the Au-coated Ag tip with the tip apex radius of ~10 nm at the 53° angle of incidence. The emitted PL signals were collected using the same objective (100×, NA 0.7, f = 200). The radius of the laser focal spot was ~500 nm. AFM measurements were performed in the tapping mode with the 20 nm average TSD. TEPL measurements were performed in the AFM contact mode. The angle between the incident laser optical axis and the horizontal sample plane was 25°. The angle between the tip and the sample plane was 78°. The incident light polarization was along the tip axis. The tip and the laser were stationary during the experiments, while the sample stage was scanned.

Monolayer thickness of 2D heterostructures was confirmed by AFM and Raman measurements (not shown) as previously described.[42] Briefly, Raman characterization measurements were performed using 532 nm excitation. The observed Raman intensity of the MoS_2 in-plane $E^1{}_{2g}$ vibrational mode at 385 cm^{-1} was in agreement with the previously reported monolayer MoS_2.[40] Similarly, the vibrational mode at 355 cm^{-1} confirmed the presence of monolayer WS_2.[41] AFM height profiles showed an average monolayer thickness of ~0.9 nm.[41]

Experimental results

Fig. 1 shows the sketch of the experimental setup and schematic diagrams illustrating the measured PL signals. Fig. 1a shows a schematic monolayer lateral WS_2–MoS_2 heterostructure with different tip locations on the MoS_2 (left), WS_2 (right), and center of the WS_2–MoS_2 junction (middle). Three tips at different TSDs are shown at each location. These TSDs correspond to the non-contact (large TSD > 1 nm), van der Waals (vdW) contact (medium TSD = 0.36 nm), and conductive contact (small TSD < 0.22 nm). Quantum tunneling takes place at TSD smaller than the vdW contact distance. Therefore, it is referred to as the quantum regime. The large TSD range is referred to as the classical regime. The spatial resolution of the PL imaging in the classical regime varies from the far-field excitation spot size of ~ 500 nm radius shown by the red oval in Fig. 1a to the the near-field excitation spot size based on the 10 nm radius of the tip apex. The spatial resolution in the quantum regime is given by the size of the single gold atom at the tip apex.

The sketch of the TEPL setup in Fig. 1c shows the plasmonic Au tip on top of the WS_2–MoS_2 heterostructure. The area used for TEPL measurements (blue box) includes parts of the pure WS_2, MoS_2, and the WS_2–MoS_2 junction. The inset shows the AFM phase image with marked locations of TSD measurements labeled 1–9, where spot 3 is on the junction. We chose

Open Access Article. Published on 30 2023. Downloaded on 02-08-2024 18:17:53.
This article is licensed under a Creative Commons Attribution-NonCommercial 3.0 Unported Licence.

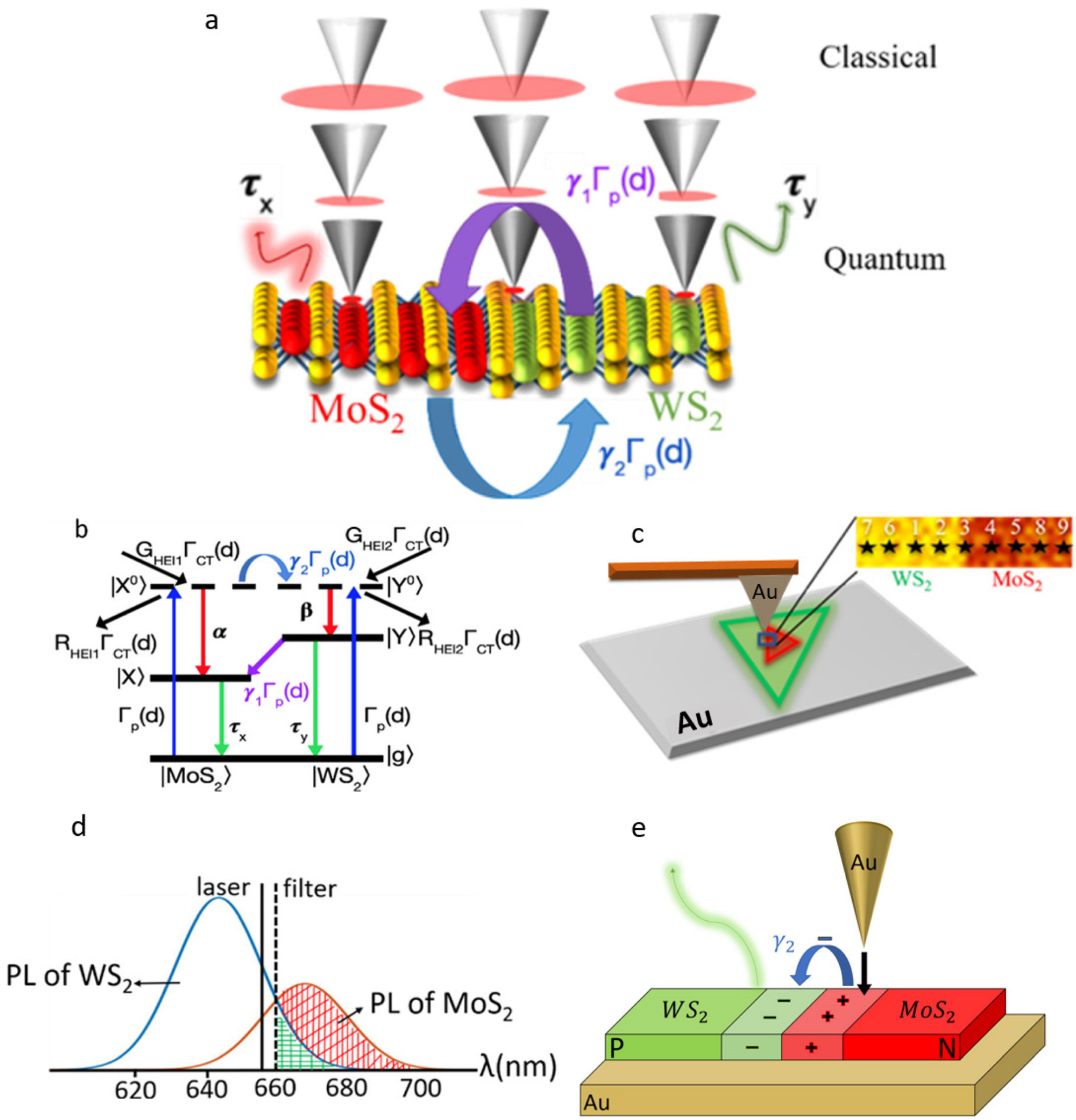

Fig. 1 (a) Sketch of the tip–sample distance (TSD) dependence PL measurements of a lateral WS$_2$–MoS$_2$ heterostructure in the classical (TSD > 0.36 nm) and quantum (TSD < 0.36 nm) regimes. Electric field excitation spots (red ovals) decrease with the decrease of TSD. (b) The schematic energy level diagram of the 2D lateral heterojunction shows hot electron injection (HEI) from the plasmonic tip to the heterostructure accompanied by the nonresonant (γ_1, purple arrow) and resonant (γ_2, blue arrow) charge transfer. (c) Tip–sample configuration in tip-enhanced photoluminescence (TEPL) experiments. Inset shows an AFM phase image of a part of the heterostructure including the WS$_2$–MoS$_2$ junction and locations 1–9 of TSD measurements. (d) Sketch of the PL signals of WS$_2$ (green shaded area) and MoS$_2$ (red shaded area) including the laser (solid line) and the filter cutoff (dashed line). (e) Schematic diagram of the PL enhancement mechanism in a quantum plasmonic p–n junction.

representative spots 1–5 for the analysis below. Other spots located further away from the junction showed similar behavior that is characteristic of the pure WS$_2$ and MoS$_2$ materials. The distances between the spots 1–2, 2–3, 3–4, and 4–5 are 172 nm, 246 nm, 238 nm, and 231 nm, respectively.

We used a 660 nm excitation laser with a 665 nm cutoff spectral filter to block the laser background as shown in Fig. 1d. This resulted in the partial cutoff of the WS$_2$ and MoS$_2$ PL signals shown by the highlighted green and red shaded spectral areas in Fig. 1d, respectively. No filter was used for the corresponding PL spectra obtained with 532 nm excitation (see ESI Fig. S1 and S2†).

TSD dependent PL measurements at the S1–S5 locations across the WS$_2$–MoS$_2$ junction are shown in the classical and quantum regimes in Fig. 2 and 3, respectively. The 2D contour maps in Fig. 2a–e show PL intensity as a function of TSD and

This journal is © The Royal Society of Chemistry 2023

Open Access Article. Published on 30 2023. Downloaded on 02-08-2024 18:17:53.
This article is licensed under a Creative Commons Attribution-NonCommercial 3.0 Unported Licence.

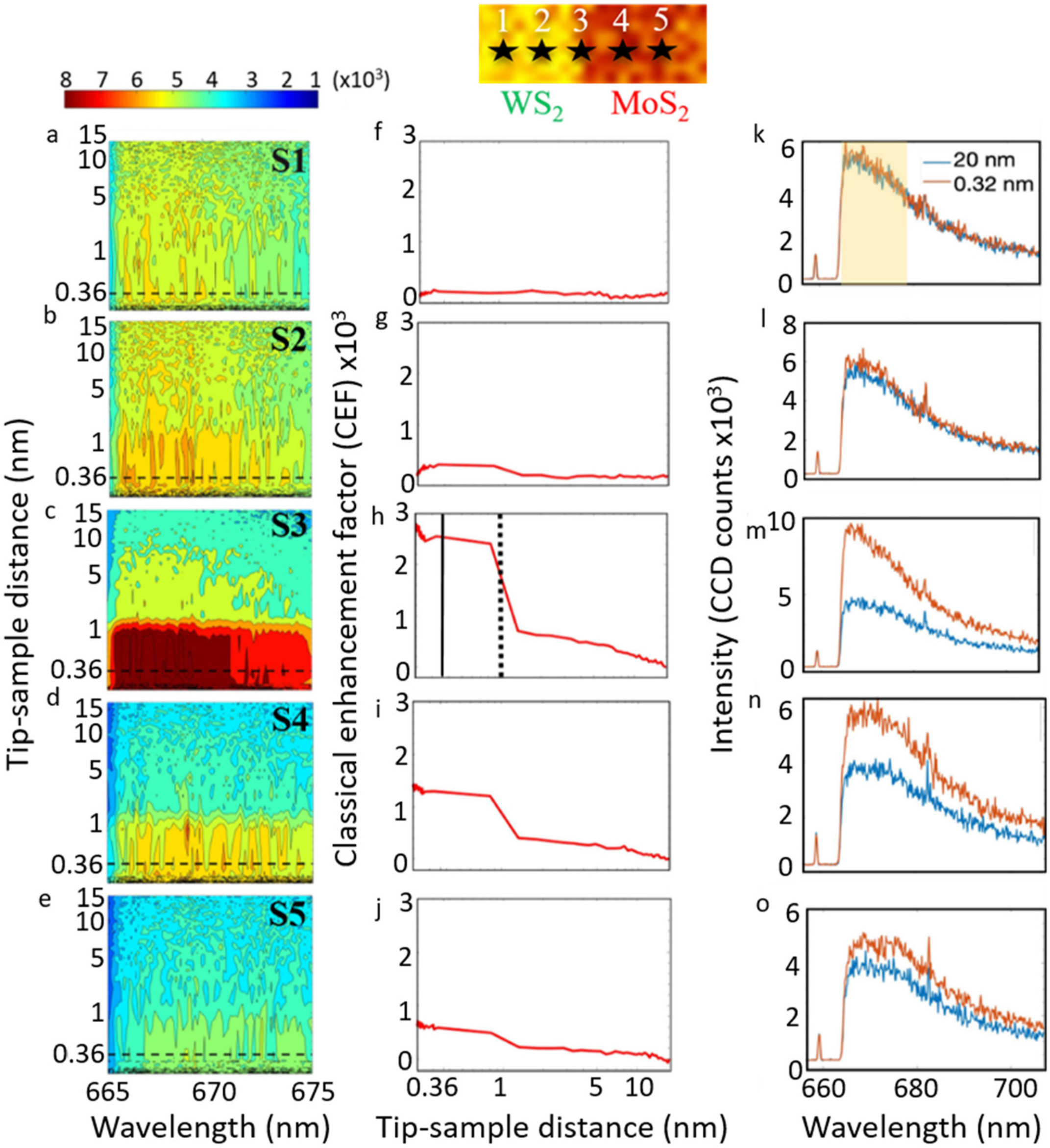

Fig. 2 Tip–sample distance (TSD) dependent PL of WS$_2$–MoS$_2$ lateral heterostructure. (a–e) 2D contour plots of PL signals at various TSDs for locations S1–S5 across the junction, shown at 5 spots in the inset (marked as stars 1–5). (f–j) Classical enhancement factors and (k–o) PL spectra at the corresponding locations. PL spectral intensities are shown at 20 nm (blue) and 0.32 nm (red) TSDs. Vertical solid and dashed lines in (h) indicate the van der Waals contact and jump-to-contact TSDs, respectively. The shaded area in (k) highlights the spectral range of the integrated TSD signal.

wavelength. The 2D contour plots were obtained by combining the PL signals at two TSD regimes, separated by the horizontal dashed lines in Fig. 2a–e. Our TSD analysis procedure was previously described.[26] Briefly, we used the TSD = 0.36 nm as a reference point, which corresponds to the vdW contact distance between the Au atom of the tip and the S atom of the WS$_2$–MoS$_2$ heterostructure. We used the piezo motor positions as TSD values in the classical regime (above the horizontal dashed line). The TSD values in the quantum regime (below the dashed line) were obtained using our previously described fitting procedure in the repulsive range of the Lennard-Jones potential.[26] Briefly, the tip and laser were kept stationary before the vdW contact, while the sample stage moved upwards. After the vdW contact, both the tip and sample moved upwards together, while the AFM cantilever bending and the tip–sample repulsive force increased. The corresponding TSD values were obtained by fitting the repulsive force as a function of the piezo position. We used the value of the A coefficient, $A = 2.2 \times 10^{-7}$, in the repulsive force, $F = A/d^{13}$, and the cantilever spring constant of 2.8 N m^{-1}.

We calculated the classical and quantum enhancement factors, shown in Fig. 2 and 3, respectively, that provides quantitative analysis of the PL enhancement normalized by the contributing areas in the classical and quantum regimes. We use

Open Access Article. Published on 30 2023. Downloaded on 02-08-2024 18:17:53.
This article is licensed under a Creative Commons Attribution-NonCommercial 3.0 Unported Licence.

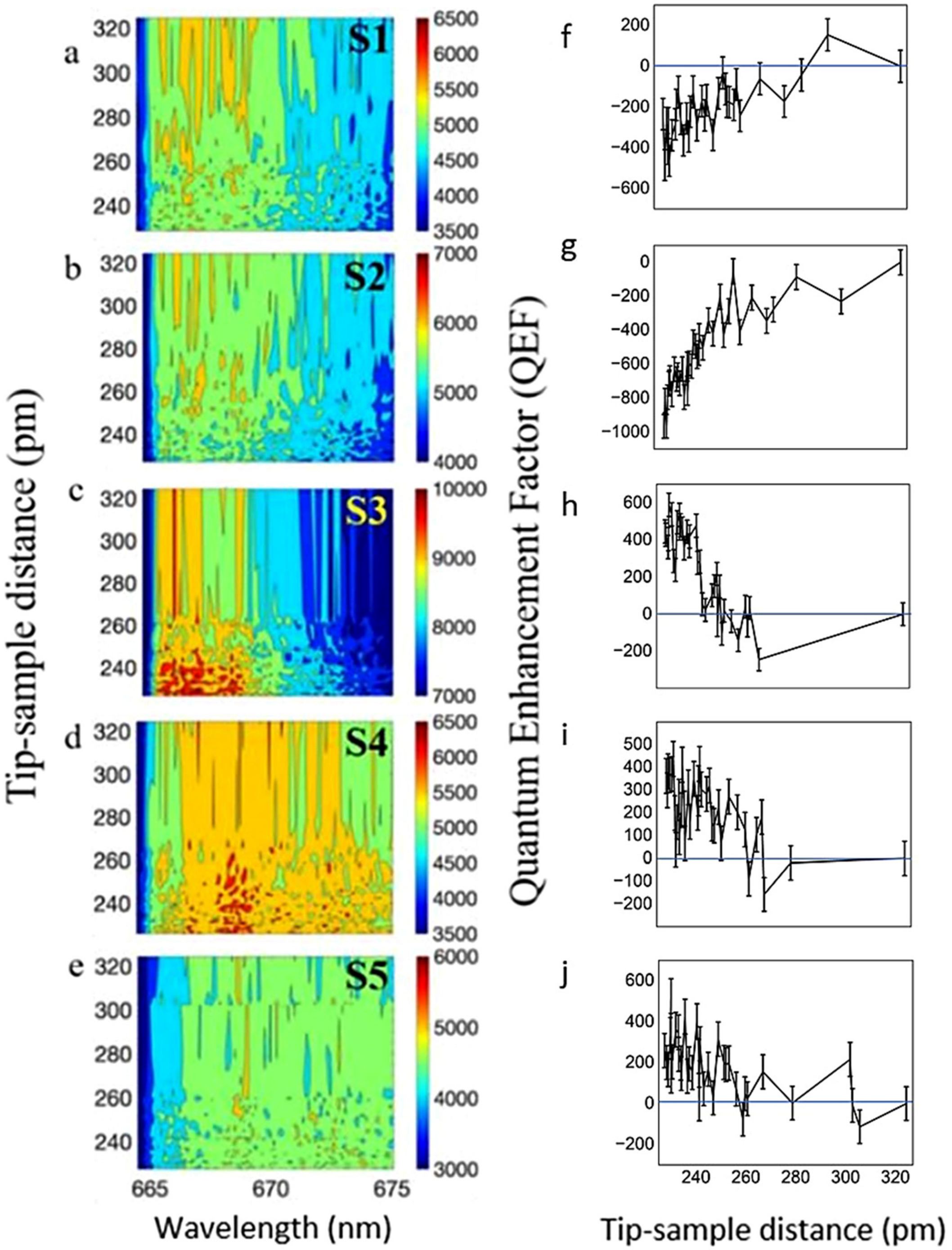

Fig. 3 Picoscale TSD dependent PL of WS_2–MoS_2 lateral heterostructure in the quantum tunneling regime. (a–e) 2D contour plots and (f–j) quantum enhancement factors for the locations S1–S5 corresponding to Fig. 2.

the conventional definition of the classical enhancement factor (CEF) as:[43]

$$\mathrm{CEF} = \left(\frac{I_{\mathrm{Tip\,In}}}{I_{\mathrm{Tip\,Out}}} - 1\right)\frac{S_{\mathrm{FF}}}{S_{\mathrm{NF}}}, \tag{1}$$

where $I_{\mathrm{Tip\ In}}$ and $I_{\mathrm{Tip\ Out}}$ are the PL intensities with the tip in contact and out of contact with the sample, respectively. S_{NF} and S_{FF} are the effective surface areas that generate the near-field (NF) and far-field (FF) PL signals, respectively. We assume that the NF PL at vdW contact is generated by the tip apex with the 10 nm radius of curvature. On the other hand, the radius of the FF excitation laser spot is ~500 nm. Assuming circular areas of πR^2 for both cases gives the value of $\frac{S_{\mathrm{FF}}}{S_{\mathrm{NF}}}$ of 2.5×10^3. The resulting CEF values as a

This journal is © The Royal Society of Chemistry 2023

Open Access Article. Published on 30 2023. Downloaded on 02-08-2024 18:17:53.
This article is licensed under a Creative Commons Attribution-NonCommercial 3.0 Unported Licence.

function of TSD are shown for the locations S1–S5 in Fig. 2f–j, respectively.

In the quantum plasmonic regime, we consider the tunneling effect by using the NF PL intensity at vdW contact TSD of 0.36 nm for I_{vdW}, relative to the NF PL at TSD < 0.32 nm for I_{C}, which approaches the conductive contact distance of 0.22 nm. The corresponding quantum EF (QEF) equation is:

$$\mathrm{QEF} = \left(\frac{I_{\mathrm{C}}}{I_{\mathrm{vdW}}} - 1\right)\frac{S_{\mathrm{vdW}}}{S_{\mathrm{C}}}. \tag{2}$$

We assume that the PL enhancement at TSD < 0.36 nm originates from only a few atoms at the tip apex, in the limit from just one Au atom. Therefore, we use the radius of a Au atom of 0.179 nm to define the area S_{C}. For S_{vdW} we use the same area as above for the near field with the tip apex area of 10 nm. This gives the value of the $\frac{S_{\mathrm{vdW}}}{S_{\mathrm{C}}}$ factor of 1.2×10^4. The resulting QEF values as a function of TSD are shown for the locations S1–S5 in Fig. 3f–j, respectively.

By setting the S_{C} area to one Au atom we obtained the highest estimate of QEF. This assumption is based on recent sub-nanometer resolution TERS and TEPL experiments, where a single Au or Ag atom protruding from a plasmonic tip was responsible for the signal enhancement.[44–48] The QEF will decrease by taking the low estimate of the tip apex area of 10 nm. However, our experimental results better match the simulations using the single Au atom area.

We compared the CEF and QEF values at the locations S1–S5 in Table 1. The CEF value at TSD = 0.32 nm provides the estimate of the relative PL enhancement due to the near field at the tip apex interacting with the various parts of the heterostructure. The largest enhancement of 2554 was obtained at the junction in spot S3. Less than 2 orders of magnitude enhancement was obtained in spot S1 on the pure WS_2. This may be attributed to the different enhancement mechanisms of the junction compared to the pure materials, as discussed below. Further suppression in spot S1 is observed in QEF by decreasing the TSD, with large negative values of QEF indicating the contribution of the traditional quantum plasmonic limit to the PL enhancement.[33,34] On the other hand, at location S3 of the junction, the QEF value is large and positive, indicating the additional three orders of magnitude PL enhancement by a further decrease of TSD by a hundred pm below the vdW contact. Positive QEF is also observed at locations S4 and S5 on pure MoS_2 with lower values compared to the junction. This enhancement decreases when the tip moves away from the junction.

Table 1 Classical (CEF) and quantum (QEF) enhancement factors at van der Waals contact (~0.32 nm) and at conductive contact (~0.20 nm) TSD, respectively, at locations S1–S5

Spots	CEF (0.32 nm)	QEF (0.20 nm)
S1	16	−234
S2	219	−966
S3	2554	445
S4	1294	362
S5	587	259

Theoretical model

We used the phenomenological rate equation model to describe the interplay between hot electron injection and charge transfer across the junction that was observed in the experiments. Fig. 1b shows the schematic state diagram used to model the excited state dynamics of the WS_2–MoS_2 heterostructure. It shows that the initial population of the electrons excited from the ground state, $|g\rangle$, above the band gap to states $|X^0\rangle$ or $|Y^0\rangle$, subsequently decays to exciton states $|X\rangle$ or $|Y\rangle$. Here, $|X^0\rangle$, $|X\rangle$ and $|Y^0\rangle$, $|Y\rangle$ are the excited states of the MoS_2 and WS_2 parts of the heterostructure, respectively, which might include some degree of alloying due to the proximity to the junction. As a result, the population dynamics can be described by the following rate equations:

$$\frac{\mathrm{d}N_{\mathrm{g}}}{\mathrm{d}t} = -2\Gamma_{\mathrm{p}}(d)N_{\mathrm{g}} + \frac{N_X}{\tau_X} + \frac{N_Y}{\tau_Y}, \tag{3}$$

$$\frac{\mathrm{d}N_X}{\mathrm{d}t} = \alpha N_{X^0} - \frac{N_X}{\tau_x} + \gamma_1\Gamma_{\mathrm{p}}(d)N_{\mathrm{Y}}, \tag{4}$$

$$\frac{\mathrm{d}N_Y}{\mathrm{d}t} = \beta N_{Y^0} - \frac{N_Y}{\tau_Y} - \gamma_1\Gamma_{\mathrm{p}}(d)N_Y, \tag{5}$$

$$\frac{\mathrm{d}N_{X^0}}{\mathrm{d}t} = \Gamma_{\mathrm{p}}(d)N_{\mathrm{g}} - \alpha N_{X^0} - \gamma_2\Gamma_{\mathrm{p}}(d)N_{X^0}, \tag{6}$$

$$N_{\mathrm{g}} + N_X + N_Y + N_{X^0} + N_{Y^0} = 1, \tag{7}$$

where $\alpha = 1\ \mathrm{ps}^{-1}$ and $\beta = 15\ \mathrm{ps}^{-1}$ are the exciton $|X\rangle$ and $|Y\rangle$ generation rates (red arrows). The larger value of β compared to α is used due to the stronger light–matter interaction of WS_2 compared to MoS_2 at the 660 nm excitation. $\tau_X = \tau_Y = 2$ ps are the average exciton lifetimes,[49] and $\Gamma_{\mathrm{p}}(d)$ is the TSD dependent near-field excitation rate, given by

$$\Gamma_{\mathrm{p}}(d) = \begin{cases} A\left(1 - \dfrac{B}{(R+d-c)^3}\right)^{-2}, & \text{for } d > 0.36\ \mathrm{nm} \\ 1 - \mathrm{e}^{-\frac{d-c}{d_{\mathrm{p}}}}, & \text{for } c < d < 0.36\ \mathrm{nm} \end{cases}, \tag{8}$$

where A is the constant of continuity, $B = 5028$ characterizes the probe's material properties,[16,27,34] $R = 10$ nm is the radius of curvature of the tip apex, $c = 0.17$ nm is the conductive ohmic contact distance, and $d_{\mathrm{p}} = 0.02$ nm is the average quantum tunneling distance.[34] Due to the junction's intrinsic chemical potential difference, electrons transfer from WS_2 to MoS_2 (purple arrow) with the rate $\gamma_1\Gamma_{\mathrm{p}}(d)$, where γ_1 is the photoinduced electron transfer coefficient.[34] Lastly, we introduce $\gamma_2\Gamma_{\mathrm{p}}(d)$ to describe the transfer of hot electrons from the plasmonic tip to the resonantly excited junction (blue arrow). The hot electrons are injected with the rate of $G_{\mathrm{HEI}}\Gamma_{\mathrm{CT}}(d)$ into the heterostructure and they relax by forming excitons at rates α or β in MoS_2 and WS_2 (red arrows), respectively, or through nonradiative decay channels at the rate of $G_{\mathrm{HEI}}\Gamma_{\mathrm{CT}}(d)$.

Open Access Article. Published on 30 2023. Downloaded on 02-08-2024 18:17:53.
This article is licensed under a Creative Commons Attribution-NonCommercial 3.0 Unported Licence.
BY-NC

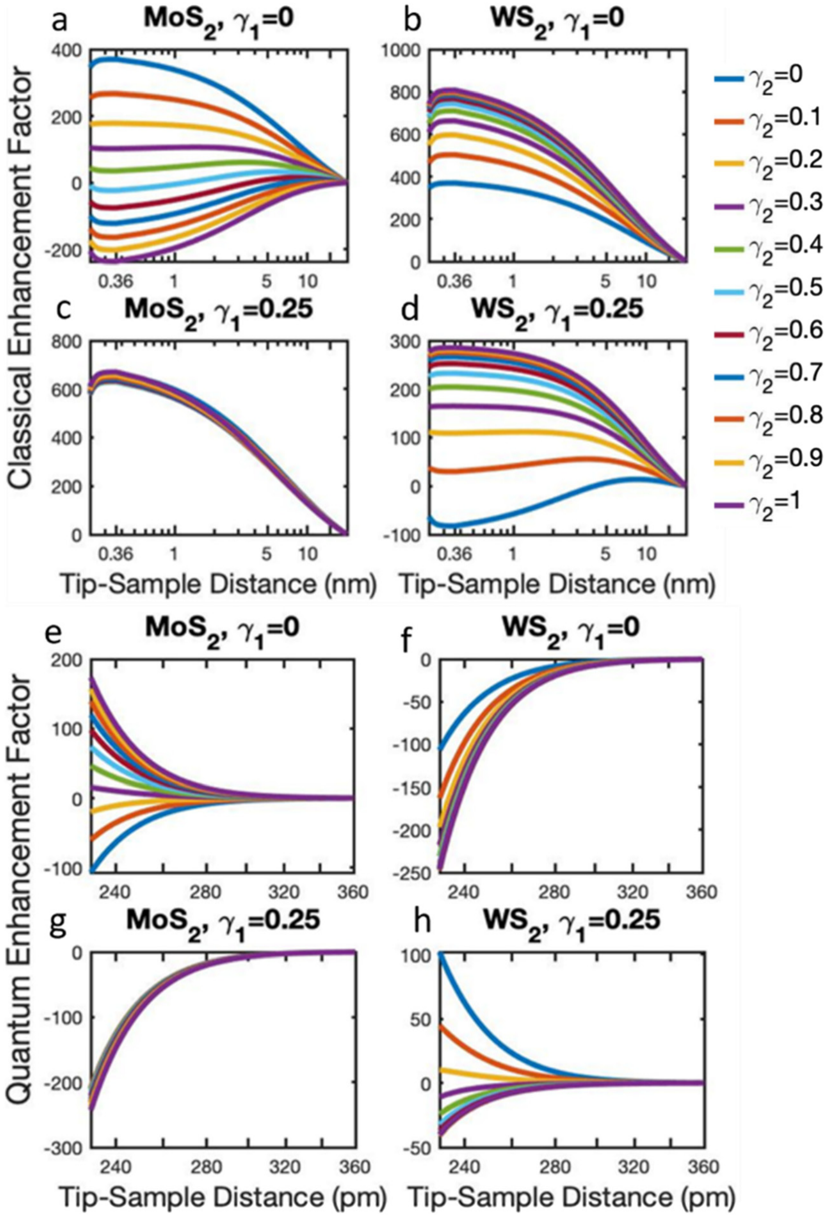

Fig. 4 Simulated classical (a–d) and quantum (e–h) TSD dependent PL enhancement factors of WS$_2$–MoS$_2$ heterostructure for various values of the nonresonant (γ_1) and resonant (γ_2) charge transfer coefficients. The PL signals for $\gamma_1 = \gamma_2 = 0$ correspond to the pure MoS$_2$ (a and e) and WS$_2$ (b and f) materials (blue lines). The PL signals for $\gamma_1 = 0.25$ correspond to the WS$_2$–MoS$_2$ junction (c, d, g and h).

Fig. 4 shows the simulated PL enhancement factors for $\gamma_1 = 0$ (a, b, e and f) and $\gamma_1 = 0.25$ (c, d, g and h) for several values of γ_2. The classical and quantum EFs were obtained using the ratios of the $|X\rangle$ and $|Y\rangle$ state populations at the TSDs corresponding to the experimental EFs defined above. The PL signals for $\gamma_1 = \gamma_2 = 0$ correspond to the pure MoS$_2$ (a and e) and WS$_2$ (b and f) materials. In both cases, the EF values increase in the classical and decrease in the quantum regimes (blue lines in Fig. 4a, b, e and f for $\gamma_1 = \gamma_2 = 0$). This behavior corresponds to the traditional classical/quantum plasmonics, and it is in good agreement with the experimental measurements at locations S1 (WS$_2$) and S5 (MoS$_2$), shown in Fig. 2f, j and 3f, j. Fig. 3j shows a small enhancement of WS$_2$ PL due to the proximity to the junction, which disappears at locations S8 and S9 further away from the junction.

Discussion

Quantum plasmonic tunneling in a picocavity suppresses the PL of pure materials both under the resonant and above the band gap excitations. This has traditionally limited the plasmonic PL enhancement. For example, exciton quenching was observed by decreasing the gap size in a Au tip – Au nanotriangle plasmonic picocavity.[50] It was attributed to the interplay of two effects, namely, the quantum plasmonic tunneling and

Open Access Article. Published on 30 2023. Downloaded on 02-08-2024 18:17:53.
This article is licensed under a Creative Commons Attribution-NonCommercial 3.0 Unported Licence.

the photoexcited charge transfer from MoS_2 to the Au tip by exciton dissociation at the Schottky barrier.

Previous work on improving the contact between 2D semiconductors and 3D metal-buried interfaces showed PL suppression by direct evaporation of Au on MoS_2.[51] This corresponds to the transition from vdW Au – MoS_2 contact to a higher quality electronic contact, which is analogous to the decrease of TSD in our experiments. Charge transfer and local strain induce degenerate doping in MoS_2. Strain may also contribute to PL modulation in our tip–sample cavity. Previous work on TEPL of nanostrained $MoSe_2$ showed the emergence of enhanced anomalous PL from a new excitonic state localized on top of a silicon nanowire.[52] However, we did not observe such a new state in our TSD experiments, and, therefore, rule out strain contribution.

Previous TEPL imaging of 2D $MoSe_2$ revealed the cumulative effect of Purcell enhancement and oxygen induced doping leading to the enhanced biexciton emission, facilitated by the increased exciton density in the highly localized tip area.[53] We did not observe any significant PL red-shift at decreasing TSD, and, therefore, ruled out the biexciton formation.

In contrast to these studies, our results showed that in TMD heterostructures it is possible to obtain an additional increase of the PL signal in the tunneling regime beyond the conventional quantum plasmonic limit. Our 660 nm excitation is near resonant with the tunneling-induced charge transfer plasmon (CTP) mode that was previously observed in a similar Au tip – Au substrate cavity.[54] The role of CTP resonance in the PL enhancement is confirmed by the comparison of the resonant 660 nm excitation, which gives the 3 orders of magnitude PL enhancement (Fig. 2 and 3) to the insignificant enhancement under the nonresonant 532 nm excitation (ESI Fig. S1 and S2†). Our 2D lateral heterostructure forms a p–n junction at the interface between the two materials due to the slightly different doping in our CVD-grown materials, with p-doped WS_2 and n-doped MoS_2 as previously described.[6] This provides an additional mechanism of PL enhancement as shown in Fig. 1e. The space charge region at the junction facilitates hot electron tunneling from the Au tip to the positively charged MoS_2, while the transfer to the negatively charged WS_2 region is suppressed. The charge transfer to MoS_2 is increased by CTP in the quantum regime, reducing the electric field of the depletion region and increasing the charge transfer γ_2 across the junction. The resulting increased carrier concentration on WS_2 enhanced the PL signal. In summary, the quantum tunneling induced CTP and quantum plasmonic p–n junction mechanisms both enhanced the PL of WS_2 (suppressed the PL of MoS_2) in the quantum regime. Previous work showed an increase of the photoinduced charge carrier generation in a p–n junction by the electromagnetic (EM) mechanism in the classical regime.[55–57] Here we attribute the tunneling in a p–n junction inside the plasmonic picocavity to a charge-transfer-based chemical mechanism (CM).[58,59] We previously showed the possibility of switching from the EM to the CM mechanism in a plasmonic picocavity by decreasing the TSD.[54] Here we extend this approach to a 2D heterojunction, providing new possibilities to control the optoelectronic properties of nanoscale devices.

This work may be extended to other 2D materials, such as the WSe_2–$MoSe_2$ heterostructure, by choosing the appropriate excitation source and plasmonic cavity. Our previous work on hot electron injection into the WSe_2–$MoSe_2$ heterojunction showed the opposite PL enhancement effects compared to this work. In contrast to the results on resonantly excited WS_2–MoS_2 heterostructure on Au substrate presented here, the previous work on WSe_2–$MoSe_2$ on SiO_2/Si substrate did not have the CTP enhancement mechanism.

The simulation in Fig. 4d shows that WS_2 PL is enhanced at the junction as TSD is decreased in the classical regime only when $\gamma_2 > 0.2$, predicting the suppression of WS_2 PL for $\gamma_2 < 0.2$ in the classical regime. In addition, Fig. 4h shows the decrease of the WS_2 PL at the junction in the quantum regime for $\gamma_2 > 0.3$, which implies the optimal value of $\gamma_2 \sim 0.25$. Our model, therefore, describes the significant contribution of the CTP resonant transfer, γ_2, whose TSD dependence is opposite to the nonresonant charge transfer, γ_1. The interplay of these mechanisms determines the optimal values of the theoretical parameters that best describe the experimental observations.

Conclusions

In summary, we performed nanoscale PL measurements of lateral monolayer WS_2–MoS_2 heterostructures and observed a large increase of PL in the regime of sub-nanometer scale tip–sample distance at the location of the heterojunction. We attributed the enhancement to the interplay of the quantum plasmonic and chemical charge transfer mechanisms in the coupled 2D materials in a plasmonic picocavity. Our simulations predicted the corresponding charge transfer rates and showed good agreement with the experiments. The plasmonic tip is shown to be an efficient nano-imaging tool as well as a novel control platform.

Author contributions

D.V.V. conceived the idea and designed the experiments. P.K.S. prepared the sample. D.V.V., J.L., and X.L. performed the experiments. D.V.V., S.A., Z.H.W., A.A., and A.Z. analyzed the data. Z.H.W. performed the simulations. All authors discussed and wrote the paper.

Conflicts of interest

There are no conflicts to declare.

References

1 C. Huang, S. Wu, A. M. Sanchez, J. J. Peters, R. Beanland, J. S. Ross, P. Rivera, W. Yao, D. H. Cobden and X. Xu,

Open Access Article. Published on 30 2023. Downloaded on 02-08-2024 18:17:53.
This article is licensed under a Creative Commons Attribution-NonCommercial 3.0 Unported Licence.

Lateral Heterojunctions within Monolayer MoSe2–WSe2 Semiconductors, *Nat. Mater.*, 2014, **13**(12), 1096–1101.

2 M.-Y. Li, Y. Shi, C.-C. Cheng, L.-S. Lu, Y.-C. Lin, H.-L. Tang, M.-L. Tsai, C.-W. Chu, K.-H. Wei and J.-H. He, Epitaxial Growth of a Monolayer WSe2-MoS2 Lateral Pn Junction with an Atomically Sharp Interface, *Science*, 2015, **349**(6247), 524–528.

3 X. Ling, Y. Lin, Q. Ma, Z. Wang, Y. Song, L. Yu, S. Huang, W. Fang, X. Zhang and A. L. Hsu, Parallel Stitching of 2D Materials, *Adv. Mater.*, 2016, **28**(12), 2322–2329.

4 M.-Y. Li, C.-H. Chen, Y. Shi and L.-J. Li, Heterostructures Based on Two-Dimensional Layered Materials and Their Potential Applications, *Mater. Today*, 2016, **19**(6), 322–335.

5 Y. Son, M.-Y. Li, C.-C. Cheng, K.-H. Wei, P. Liu, Q. H. Wang, L.-J. Li and M. S. Strano, Observation of Switchable Photoresponse of a Monolayer WSe2–MoS2 Lateral Heterostructure via Photocurrent Spectral Atomic Force Microscopic Imaging, *Nano Lett.*, 2016, **16**(6), 3571–3577.

6 P. K. Sahoo, S. Memaran, Y. Xin, L. Balicas and H. R. Gutiérrez, One-Pot Growth of Two-Dimensional Lateral Heterostructures via Sequential Edge-Epitaxy, *Nature*, 2018, **553**(7686), 63–67.

7 M. G. Stanford, P. D. Rack and D. Jariwala, Emerging Nanofabrication and Quantum Confinement Techniques for 2D Materials beyond Graphene, *npj 2D Mater. Appl.*, 2018, **2**(1), 1–15.

8 S. Z. Butler, S. M. Hollen, L. Cao, Y. Cui, J. A. Gupta, H. R. Gutiérrez, T. F. Heinz, S. S. Hong, J. Huang, A. F. Ismach, E. Johnston-Halperin, M. Kuno, V. V. Plashnitsa, R. D. Robinson, R. S. Ruoff, S. Salahuddin, J. Shan, L. Shi, M. G. Spencer, M. Terrones, W. Windl and J. E. Goldberger, Progress, Challenges, and Opportunities in Two-Dimensional Materials Beyond Graphene, *ACS Nano*, 2013, **7**(4), 2898–2926.

9 Y.-M. He, G. Clark, J. R. Schaibley, Y. He, M.-C. Chen, Y.-J. Wei, X. Ding, Q. Zhang, W. Yao, X. Xu, C.-Y. Lu and J.-W. Pan, Single Quantum Emitters in Monolayer Semiconductors, *Nat. Nanotechnol.*, 2015, **10**(6), 497–502.

10 M. Turunen, M. Brotons-Gisbert, Y. Dai, Y. Wang, E. Scerri, C. Bonato, K. D. Jöns, Z. Sun and B. D. Gerardot, Quantum Photonics with Layered 2D Materials, *Nat. Rev. Phys.*, 2022, **4**(4), 219–236.

11 W. Bao, N. J. Borys, C. Ko, J. Suh, W. Fan, A. Thron, Y. Zhang, A. Buyanin, J. Zhang and S. Cabrini, Visualizing Nanoscale Excitonic Relaxation Properties of Disordered Edges and Grain Boundaries in Monolayer Molybdenum Disulfide, *Nat. Commun.*, 2015, **6**(1), 1–7.

12 Y. Lee, S. Park, H. Kim, G. H. Han, Y. H. Lee and J. Kim, Characterization of the Structural Defects in CVD-Grown Monolayered MoS 2 Using near-Field Photoluminescence Imaging, *Nanoscale*, 2015, **7**(28), 11909–11914.

13 C. Lee, S. T. Kim, B. G. Jeong, S. J. Yun, Y. J. Song, Y. H. Lee, D. J. Park and M. S. Jeong, Tip-Enhanced Raman Scattering Imaging of Two-Dimensional Tungsten Disulfide with Optimized Tip Fabrication Process, *Sci. Rep.*, 2017, **7**(1), 1–7.

14 K. K. Smithe, A. V. Krayev, C. S. Bailey, H. R. Lee, E. Yalon, Ö. B. Aslan, M. Muñoz Rojo, S. Krylyuk, P. Taheri and A. V. Davydov, Nanoscale Heterogeneities in Monolayer MoSe2 Revealed by Correlated Scanning Probe Microscopy and Tip-Enhanced Raman Spectroscopy, *ACS Appl. Nano Mater.*, 2018, **1**(2), 572–579.

15 A. Krayev, C. S. Bailey, K. Jo, S. Wang, A. Singh, T. Darlington, G.-Y. Liu, S. Gradecak, P. J. Schuck and E. Pop, Dry Transfer of van Der Waals Crystals to Noble Metal Surfaces to Enable Characterization of Buried Interfaces, *ACS Appl. Mater. Interfaces*, 2019, **11**(41), 38218–38225.

16 K.-D. Park, O. Khatib, V. Kravtsov, G. Clark, X. Xu and M. B. Raschke, Hybrid Tip-Enhanced Nanospectroscopy and Nanoimaging of Monolayer WSe2 with Local Strain Control, *Nano Lett.*, 2016, **16**(4), 2621–2627.

17 W. Xue, P. K. Sahoo, J. Liu, H. Zong, X. Lai, S. Ambardar and D. V. Voronine, Nano-Optical Imaging of Monolayer MoSe2-WSe2 Lateral Heterostructure with Subwavelength Domains, *J. Vac. Sci. Technol., A*, 2018, **36**(5), 05G502.

18 Z. He, Z. Han, J. Yuan, A. M. Sinyukov, H. Eleuch, C. Niu, Z. Zhang, J. Lou, J. Hu, D. V. Voronine and M. O. Scully, Quantum Plasmonic Control of Trions in a Picocavity with Monolayer WS2, *Sci. Adv.*, 2019, **5**(10), eaau8763.

19 L. Novotny and B. Hecht, *Principles of Nano-Optics*, Cambridge university press, 2012.

20 R. Esteban, A. G. Borisov, P. Nordlander and J. Aizpurua, Bridging Quantum and Classical Plasmonics with a Quantum-Corrected Model, *Nat. Commun.*, 2012, **3**(1), 1–9.

21 J. Zuloaga, E. Prodan and P. Nordlander, Quantum Description of the Plasmon Resonances of a Nanoparticle Dimer, *Nano Lett.*, 2009, **9**(2), 887–891.

22 W. Zhu and K. B. Crozier, Quantum Mechanical Limit to Plasmonic Enhancement as Observed by Surface-Enhanced Raman Scattering, *Nat. Commun.*, 2014, **5**(1), 1–8.

23 M. S. Tame, K. R. McEnery, Ş. Özdemir, J. Lee, S. A. Maier and M. S. Kim, Quantum Plasmonics, *Nat. Phys.*, 2013, **9**(6), 329–340.

24 N. J. Halas, S. Lal, W.-S. Chang, S. Link and P. Nordlander, Plasmons in Strongly Coupled Metallic Nanostructures, *Chem. Rev.*, 2011, **111**(6), 3913–3961.

25 J. A. Scholl, A. García-Etxarri, A. L. Koh and J. A. Dionne, Observation of Quantum Tunneling between Two Plasmonic Nanoparticles, *Nano Lett.*, 2013, **13**(2), 564–569.

26 Y. Zhang, D. V. Voronine, S. Qiu, A. M. Sinyukov, M. Hamilton, Z. Liege, A. V. Sokolov, Z. Zhang and M. O. Scully, Improving Resolution in Quantum Subnanometre-Gap Tip-Enhanced Raman Nanoimaging, *Sci. Rep.*, 2016, **6**(1), 1–9.

27 V. Kravtsov, S. Berweger, J. M. Atkin and M. B. Raschke, Control of Plasmon Emission and Dynamics at the Transition from Classical to Quantum Coupling, *Nano Lett.*, 2014, **14**(9), 5270–5275.

28 K. J. Savage, M. M. Hawkeye, R. Esteban, A. G. Borisov, J. Aizpurua and J. J. Baumberg, Revealing the Quantum Regime in Tunnelling Plasmonics, *Nature*, 2012, **491**(7425), 574–577.

This journal is © The Royal Society of Chemistry 2023

Open Access Article. Published on 30 2023. Downloaded on 02-08-2024 18:17:53. This article is licensed under a Creative Commons Attribution-NonCommercial 3.0 Unported Licence.

29 W. Zhu, R. Esteban, A. G. Borisov, J. J. Baumberg, P. Nordlander, H. J. Lezec, J. Aizpurua and K. B. Crozier, Quantum Mechanical Effects in Plasmonic Structures with Subnanometre Gaps, *Nat. Commun.*, 2016, **7**(1), 1–14.

30 V. Kulkarni and A. Manjavacas, Quantum Effects in Charge Transfer Plasmons, *ACS Photonics*, 2015, **2**(7), 987–992.

31 D. Xu, X. Xiong, L. Wu, X.-F. Ren, C. E. Png, G.-C. Guo, Q. Gong and Y.-F. Xiao, Quantum Plasmonics: New Opportunity in Fundamental and Applied Photonics, *Adv. Opt. Photonics*, 2018, **10**(4), 703–756.

32 C. Ciracì, R. T. Hill, J. J. Mock, Y. Urzhumov, A. I. Fernández-Domínguez, S. A. Maier, J. B. Pendry, A. Chilkoti and D. R. Smith, Probing the Ultimate Limits of Plasmonic Enhancement, *Science*, 2012, **337**(6098), 1072–1074.

33 Y. Zhang, D. V. Voronine, S. Qiu, A. M. Sinyukov, M. Hamilton, Z. Liege, A. V. Sokolov, Z. Zhang and M. O. Scully, Improving Resolution in Quantum Subnanometre-Gap Tip-Enhanced Raman Nanoimaging, *Sci. Rep.*, 2016, **6**, 25788.

34 C. Tang, Z. He, W. Chen, S. Jia, J. Lou and D. V. Voronine, Quantum Plasmonic Hot-Electron Injection in Lateral WS e2/MoSe2 Heterostructures, *Phys. Rev. B*, 2018, **98**(4), 041402.

35 A. Albagami, S. Ambardar, H. Hrim, P. K. Sahoo, Y. Emirov, H. R. Gutiérrez and D. V. Voronine, Tip-Enhanced Photoluminescence of Freestanding Lateral Heterobubbles, *ACS Appl. Mater. Interfaces*, 2022, **14**(8), 11006–11015.

36 T. P. White and K. R. Catchpole, Plasmon-Enhanced Internal Photoemission for Photovoltaics: Theoretical Efficiency Limits, *Appl. Phys. Lett.*, 2012, **101**(7), 073905.

37 Y. Shi, J. Wang, C. Wang, T.-T. Zhai, W.-J. Bao, J.-J. Xu, X.-H. Xia and H.-Y. Chen, Hot Electron of Au Nanorods Activates the Electrocatalysis of Hydrogen Evolution on MoS2 Nanosheets, *J. Am. Chem. Soc.*, 2015, **137**(23), 7365–7370.

38 T. Hartman, C. S. Wondergem, N. Kumar, A. van den Berg and B. M. Weckhuysen, Surface-and Tip-Enhanced Raman Spectroscopy in Catalysis, *J. Phys. Chem. Lett.*, 2016, **7**(8), 1570–1584.

39 M. L. Brongersma, N. J. Halas and P. Nordlander, Plasmon-Induced Hot Carrier Science and Technology, *Nat. Nanotechnol.*, 2015, **10**(1), 25–34.

40 C. Clavero, Plasmon-Induced Hot-Electron Generation at Nanoparticle/Metal-Oxide Interfaces for Photovoltaic and Photocatalytic Devices, *Nat. Photonics*, 2014, **8**(2), 95–103.

41 J. S. DuChene, B. C. Sweeny, A. C. Johnston-Peck, D. Su, E. A. Stach and W. D. Wei, Prolonged Hot Electron Dynamics in Plasmonic-Metal/Semiconductor Heterostructures with Implications for Solar Photocatalysis, *Angew. Chem., Int. Ed.*, 2014, **53**(30), 7887–7891.

42 S. Ambardar, R. Kamh, Z. H. Withers, P. K. Sahoo and D. V. Voronine, Coupling Nanobubbles in 2D Lateral Heterostructures, *Nanoscale*, 2022, **14**(22), 8050–8059.

43 B. Pettinger, P. Schambach, C. J. Villagómez and N. Scott, Tip-Enhanced Raman Spectroscopy: Near-Fields Acting on a Few Molecules, *Annu. Rev. Phys. Chem.*, 2012, **63**, 379–399.

44 R. Zhang, Y. Zhang, Z. C. Dong, S. Jiang, C. Zhang, L. G. Chen, L. Zhang, Y. Liao, J. Aizpurua, Y. Luo, J. L. Yang and J. G. Hou, Chemical Mapping of a Single Molecule by Plasmon-Enhanced Raman Scattering, *Nature*, 2013, **498**(7452), 82–86.

45 J. Lee, K. T. Crampton, N. Tallarida and V. A. Apkarian, Visualizing Vibrational Normal Modes of a Single Molecule with Atomically Confined Light, *Nature*, 2019, **568**(7750), 78–82.

46 B. Yang, G. Chen, A. Ghafoor, Y. Zhang, Y. Zhang, Y. Zhang, Y. Luo, J. Yang, V. Sandoghdar, J. Aizpurua, Z. Dong and J. G. Hou, Sub-Nanometre Resolution in Single-Molecule Photoluminescence Imaging, *Nat. Photonics*, 2020, **14**(11), 693–699.

47 Y. Zhang, Z.-C. Dong and J. Aizpurua, Theoretical Treatment of Single-Molecule Scanning Raman Picoscopy in Strongly Inhomogeneous near Fields, *J. Raman Spectrosc.*, 2021, **52**(2), 296–309.

48 J.-Z. Zhu, G. Chen, T. Ijaz, X.-G. Li and Z.-C. Dong, Influence of an Atomistic Protrusion at the Tip Apex on Enhancing Molecular Emission in Tunnel Junctions: A Theoretical Study, *J. Chem. Phys.*, 2021, **154**(21), 214706.

49 C. Robert, D. Lagarde, F. Cadiz, G. Wang, B. Lassagne, T. Amand, A. Balocchi, P. Renucci, S. Tongay and B. Urbaszek, Exciton Radiative Lifetime in Transition Metal Dichalcogenide Monolayers, *Phys. Rev. B*, 2016, **93**(20), 205423.

50 M. Ferrera, M. Rahaman, S. Sanders, Y. Pan, I. Milekhin, S. Gemming, A. Alabastri, F. Bisio, M. Canepa and D. R. T. Zahn, Controlling Excitons in the Quantum Tunneling Regime in a Hybrid Plasmonic/2D Semiconductor Interface, *Appl. Phys. Rev.*, 2022, **9**(3), 031401.

51 K. Jo, P. Kumar, J. Orr, S. B. Anantharaman, J. Miao, M. J. Motala, A. Bandyopadhyay, K. Kisslinger, C. Muratore, V. B. Shenoy, E. A. Stach, N. R. Glavin and D. Jariwala, Direct Optoelectronic Imaging of 2D Semiconductor–3D Metal Buried Interfaces, *ACS Nano*, 2021, **15**(3), 5618–5630.

52 T. Chowdhury, K. Jo, S. B. Anantharaman, T. H. Brintlinger, D. Jariwala and T. J. Kempa, Anomalous Room-Temperature Photoluminescence from Nanostrained MoSe2 Monolayers, *ACS Photonics*, 2021, **8**(8), 2220–2226.

53 D. Moore, K. Jo, C. Nguyen, J. Lou, C. Muratore, D. Jariwala and N. R. Glavin, Uncovering Topographically Hidden Features in 2D MoSe2 with Correlated Potential and Optical Nanoprobes, *npj 2D Mater. Appl.*, 2020, **4**(1), 1–7.

54 H. N. Hrim, S. Ambardar, A. Albagami, S. Mendenhall, M. T. Trinh and D. V. Voronine, Switching from Electromagnetic to Chemical Mechanism in Quantum Plasmonic Tip-Induced Graphene Oxide Enhanced Raman Scattering, *Phys. Rev. B*, 2022, **106**(3), 035410.

55 P. Alonso-González, P. Albella, M. Schnell, J. Chen, F. Huth, A. García-Etxarri, F. Casanova, F. Golmar, L. Arzubiaga,

Open Access Article. Published on 30 2023. Downloaded on 02-08-2024 18:17:53.
This article is licensed under a Creative Commons Attribution-NonCommercial 3.0 Unported Licence.

L. E. Hueso, J. Aizpurua and R. Hillenbrand, Resolving the Electromagnetic Mechanism of Surface-Enhanced Light Scattering at Single Hot Spots, *Nat. Commun.*, 2012, **3**(1), 684.

56 M. Moskovits, Surface-Enhanced Spectroscopy, *Rev. Mod. Phys.*, 1985, **57**(3), 783.

57 G. C. Schatz and R. P. Van Duyne, Image, Field Theory of Enhanced Raman Scattering by Molecules Adsorbed on Metal Surfaces: Detailed Comparison with Experimental Results, *Surf. Sci.*, 1980, **101**(1–3), 425–438.

58 H. Xu, L. Xie, H. Zhang and J. Zhang, Effect of Graphene Fermi Level on the Raman Scattering Intensity of Molecules on Graphene, *ACS Nano*, 2011, **5**(7), 5338–5344.

59 L. Jensen, C. M. Aikens and G. C. Schatz, Electronic Structure Methods for Studying Surface-Enhanced Raman Scattering, *Chem. Soc. Rev.*, 2008, **37**(5), 1061–1073.

This journal is © The Royal Society of Chemistry 2023